Available online at www.sciencedirect.com

ScienceDirect

Energy Procedia 114 (2017) 3237 – 3246

Energy Procedia

13th International Conference on Greenhouse Gas Control Technologies, GHGT-13, 14-18 November 2016, Lausanne, Switzerland

Quantification of viscous creep influence on storage capacity of caprock

Ludovic Räss[a]*, Roman Y. Makhnenko[b,c], Yuri Podladchikov[a], Lyesse Laloui[b]

[a]*Institute of Earth Sciences, University of Lausanne, Geopolis UNIL-Mouline, CH-1015 Lausanne, Switzerland*
[b]*Laboratory of Soil Mechanics, École Polytechnique Fédérale de Lausanne, EPFL ENAC IIC LMS, GC – Station 18, CH-1015 Lausanne, Switzerland*
[c]*Department of Civil & Environmental Engineering, University of Illinois at Urbana-Champaign, 205 North Mathews Ave, Urbana, IL, 61801-2352, USA*

Abstract

In the light of growing concerns for the climate change, it is of particular interest for governments to encourage efficient capture and safe storage of large amounts of carbon dioxide in the subsurface. In this perspective and in order to accurately predict the short and long-term response of the reservoir, a precise characterization of the geomechanical properties has to be carried out. In addition to the classical poroelastic properties, time-dependent deformation, such as viscous creep should also be considered. Storage capacity of a caprock may be seriously affected by local creep deformation allowing fast vertical fluid flow through an a priori very impermeable formation. Within this study, we investigate the ease to creep of Opalinus clay (Jurassic shale) under shallow geological storage conditions and predict the propagation of high porosity channels at operational time scales. The effective poroviscoelastic parameters of rock are inferred from the novel laboratory experiments that allow evaluation of time-dependent deformation. The bulk viscosity of the shale is found to be ~ 10^{14} - 10^{15} Pa·s and it decreases with rise of temperature and pore fluid pressure to total mean stress ratio. Furthermore, the propagation speed of high porosity channels (porosity waves) is calculated to be on the order of the centimeters per year.

Peer-review under responsibility of the organizing committee of GHGT-13.

Keywords: geomechanics; shale; Opalinus clay; poromechanics; bulk viscosity; porosity waves; numerical modeling; GPU.

* Corresponding author. Tel.: +41 21 692 44 19
E-mail address: ludovic.raess@unil.ch

Peer-review under responsibility of the organizing committee of GHGT-13.
doi:10.1016/j.egypro.2017.03.1455

1. Introduction

Carbon dioxide (CO_2) storage security is largely influenced by the caprock integrity, especially at the early stages after the start of injection. The lower boundary of the caprock will then be in contact with CO_2-rich brine or pore fluid that consists almost of pure CO_2. Thermal and chemical interactions between the pore fluid and the caprock may change the material properties of the latter one. Geomechanical stability is also crucial for the caprock, since failure would potentially lead to a significant permeability increase and induced seismicity [1]. Considering clay-rich materials (e.g., shales) as potential seals has several advantages. In case the reservoir overpressure is not very important, the thermal, chemical and inelastic deformations of the clay-rich ductile formation might not affect the caprock integrity. Another advantage of considering clay-rich materials as a potential seal is that the upward movement of CO_2 through the pore system is resisted by capillary pressure; the breakthrough pressure (CO_2 entry pressure) for shale is on the order of mega Pascals [2, 3, 4].

Although clay-rich formations show interesting self-sealing features, their ease to flow (or creep) might become a serious issue when assessing long-term storage integrity of a reservoir [5]. Viscous (time-dependent) deformation of shales has been considered experimentally [e.g., 6, 7, 8], but little attention was payed to studying material behavior at high pore pressures as it is in geological storage. In general, geomaterials, even partially saturated with water, have a nonlinear rheology and time-dependent behavior of rock is a function of mean and differential stress, pore pressure, chemistry of a pore fluid, temperature, and microstructural properties of the rock among others [e.g. 9, 10, 11].

Viscous compaction of fluid-filled porous media allows a generation of a special type of fluid flow instability that leads to formation of high-porosity, high-permeability domains that are able to self-propagate upwards due to interplay between buoyancy and viscous resistance of the deforming porous matrix. This instability is known as “porosity wave” [12, 13] and its formation is possible under conditions applicable to carbon dioxide storage in reservoirs and explains creation of high-porosity channels and chimneys [14].

In this study, time-dependent or poroviscoelastic processes are included in the constitutive equations by analogy with Biot’s poroelastic relationships. We present the experimental methods to measure the parameters related to the model and the values of this parameters at in situ conditions for a caprock representative - Opalinus clay (Jurassic shale). We use the values obtained in the lab experiments to feed the numerical models in order to predict the time and length scale of possible porosity wave propagation in conditions relevant for caprock integrity.

2. Background

To predict the porosity evolution, thus the possible formation of high permeability and porosity pipe structures in saturated porous media, we use a closed system of equation proposed by [15] were time dependent or creep effects are taken into account using the viscoelastic correspondence principle. The model reduces to Biot linear theory in the elastic limit [16] and verifies the viscous solution in the incompressible limit [17]. The set of proposed equations forms a closed system that ensures thermodynamic consistency and non-negativity of entropy production. Within this section, we highlight some relevant parts of the full derivation that can be found in [15].

The variable ϕ represents the interconnected porosity, υ^s and υ^f are solid and fluid velocity, respectively. Fluid and solid pressures, p^f and p^s respectively, can be expressed through the fluid bulk modulus K_f, the unjacketed bulk modulus K_s', and the unjacketed pore bulk modulus K_s'' [18]. The main rheological assumption adopted here is the Maxwell bulk viscoelasticity:

$$\nabla_k v_k^s = -\frac{1}{K_d}\frac{\partial \bar{p}}{\partial t} + \left(\frac{1}{K_d} - \frac{1}{K_s'}\right)\frac{\partial p^f}{\partial t} - \frac{\bar{p} - p^f}{(1-\phi)\eta_\phi} \tag{1}$$

Here, K_d is the drained bulk modulus and η_ϕ is the effective bulk viscosity, which reflects properties of porous rock such as its pore structure and viscous and failure parameters of its mineral grains. The viscous part is governed by the Terzaghi effective stress: $p^e = \bar{p} - p^f$. Substituting equation (1) into the solid mass balance equation provides an expression for viscous and elastic evolution of the porosity [15, 18]:

$$\frac{\partial \phi}{\partial t} = -\left(\frac{1-\phi}{K_d} - \frac{1}{K_s'}\right)\frac{\partial p_e}{\partial t} + \phi\left(\frac{1}{K_s'} - \frac{1}{K_s''}\right)\frac{\partial p^f}{\partial t} - \frac{p_e}{\eta_\phi} \tag{2}$$

The increment of fluid content is recovered by substituting equation (1) into the sum of fluid and solid mass balance equations to eliminate the time derivatives of densities and the porosity and the divergence of solid velocity [15]:

$$\nabla_j\left(\phi\left(v_k^f - v_k^s\right)\right) = \left(\frac{1}{K_d} - \frac{1}{K_s'}\right)\left(\frac{\partial \bar{p}}{\partial t} - \frac{1}{B}\frac{\partial p^f}{\partial t}\right) + \frac{p_e}{(1-\phi)\eta_\phi} \tag{3}$$

where B is Skempton's [18, 19] coefficient:

$$B = \frac{\frac{1}{K_d} - \frac{1}{K_s'}}{\frac{1}{K_d} - \frac{1}{K_s'} + \phi\left(\frac{1}{K_f} - \frac{1}{K_s''}\right)} \tag{4}$$

3. Methods

3.1 Experimental technique

The parameters introduced in section 2 that govern poroelastic behavior of isotropic fluid-saturated rock, i.e. the drained bulk modulus K_d, the unjacketed bulk modulus K_s', and Skempton's coefficient B, can be measured experimentally under the three limiting conditions: drained, unjacketed, and undrained [18]. Another unjacketed parameter - K_s'' is rarely reported, because its measurements are associated with very small pore volume changes under constant effective stress. Although, it can be calculated from equation (4) if other parameters are known.

K_s' is measured under the unjacketed boundary conditions, which are achieved in hydrostatic ($\sigma_1 = \sigma_2 = \sigma_3 = \bar{p}$ compression experiments [20]. Prismatic specimen (50 × 35 × 35 mm) with strain gage rosettes on its sides is saturated with the confining fluid (hydraulic oil), which seemed to have no chemical effect on the tested rock in a short-term. After at least 10 days of gradual increase of pore pressure up to 60 MPa, unjacketed unloading ($\bar{p} = p^f$ and $d\bar{p} = dp^f$) is performed.

Drained (constant pore pressure) and undrained (constant fluid content) compression experiments are conducted on cylindrical specimens (height = 100mm and diameter = 50 mm) in the GDS Advanced triaxial cell at the EPFL. The setup is calibrated for testing of fluid-saturated rock at elevated temperatures (Fig. 1). Back pressure saturation technique (described in [21]) is implemented: the increments of pore (or back) pressure are applied while keeping the effective mean stress approximately the same. Then, so-called *B*-checks are performed and achievement of constant value of B independent of the magnitude of the pore pressure indicates full saturation. Measured Skempton's B coefficient values are corrected to consider the contribution of the "dead" volume and the compressibility of the pore pressure measuring system. Drained bulk modulus K is calculated directly from the measured axial and radial displacements and indirectly from the volume of the fluid that escaped the specimen during compression under constant pore pressure. Knowledge of K_s' then can provide a proper evaluation of K [18].

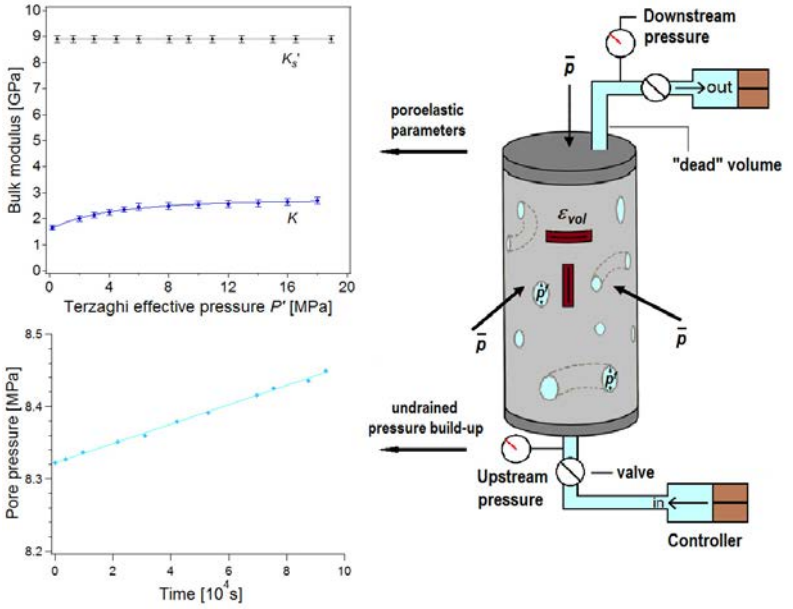

Fig 1. Experimental setup within the Advanced triaxial cell at the EPFL with indication of performed measurements; precise stress and strain measurements at different limiting regimes allow for calculation of poroelastic parameters and observation of undrained pore-pressure build-up for fully saturated specimens provides the evaluation of material's bulk viscosity.

Equation (1) provides the following method for calculating the bulk viscosity under constant mean stress, $d\bar{p}/dt = 0$, and drained boundary conditions, $dp^f/dt = 0$, which can be referred to as the "direct" method,

$$\eta_\phi = -\frac{\bar{p} - p^f}{(1-\phi)\nabla_k \upsilon_k^s} \tag{5}$$

Here $\nabla_k \upsilon_k^s$ can be treated as the volume strain rate, and considering the accuracy of volume strain measurements (1×10^{-5}) and the level of applied effective mean stresses (~ MPa), the observation time for calculating the bulk viscosity with two significant figures is ~ 10^5 sec. The time scales should be even longer to compensate for the effects of temperature and pressure perturbations; hence the bulk viscosity of shallow rock is rarely reported.

For porous materials, the degree of saturation is the critical parameter to govern their viscous response: if saturation is not full – pore pressure does not increase significantly under the undrained condition, but rather decreases while the air bubbles dissolve in pore water. However, when the full saturation is achieved and material deformation can be considered poroviscoelastic, then equation (3) predicts pore pressure build-up with time at constant total stress conditions. Changes in pore pressure for the fully saturated specimens can be measured more accurately than volume strain; hence, it can be used as the monitoring parameter for viscous behavior and for the calculation of bulk viscosity [22]. The simplified form of equations (2) and (3) for the case of undrained deformation (no flow condition: $\nabla_j\left(\phi\left(\upsilon_j^f - \upsilon_j^s\right)\right) = 0$) at constant mean stress ($d\bar{p}/dt = 0$) leads to another method (referred as "indirect") of evaluating η_ϕ,

$$\eta_\phi = \frac{B\left(\bar{p} - p^f\right)}{(1-\phi)\dfrac{dp^f}{dt}\left(\dfrac{1}{K_d} - \dfrac{1}{K_s'}\right)} \tag{6}$$

The bulk viscosity calculation then requires accurate measurements of poroelastic parameters. However, due to the accuracy of pore pressure measurements this method is significantly less time consuming (~ 10^4 sec).

3.2 Numerical methods

Numerically, the system of partial differential equations is solved on a three-dimensional (3D) staggered grid with regular grid spacing, using a finite difference (FD) discretization. Pressures and material properties are defined at the cell centers, while the Darcy fluxes and solid velocities are defined at the cell mid-faces. Shear components are located at the cell corners. The 3D model is written in C language with CUDA features and is solved on many graphical processing units (GPUs) in parallel, using the standard Message Passing Interface (MPI) routine for inter processes communications.

An iterative pseudo-transient, thus matrix-free, scheme is used to solve the system of partial differential equations. The advantages of using this approach are the lowest possible memory usage that scales O(n) while only local stencil operation to update variables and minimum point to point communication between parallel processes are needed. Such algorithm, therefore, scales linearly with number of parallel processors due to and ensured by its minimalistic construction.

The workflow of the algorithm can be summarized in the following steps, that will be repeated within the time step loop: 1) update values of total and fluid pressures and porosity solving for their time derivatives in the equations (1), (2), and (3); 2) compute the nonlinear viscoelastic rheology as function of the updated porosity and pressures fields; 3) solve the momentum equation (force balance) for the solid velocities; 4) verify the nonlinear residual of the momentum equation and the errors of the equations (1) – (3) and of the nonlinear rheology. Once step 4) is verified and all errors converged to targeted nonlinear tolerance, the porosity can be explicitly advected using a flux limiting upwind scheme [23].

The nonlinear nature of the poroviscoelastic equations sets important challenges in terms of numerical solutions. Strong localization in space and time might spontaneously occur, and a wide range of length scales are involved. To overcome this and to resolve the instabilities, a very high resolution in space and time is required to predict accurate system evolution in time. We therefore employ a numerical resolution of more than $2.5 \cdot 10^8$ grid points in order to have 500 x 500 x 1000 cells in x, y, and z directions, respectively. The GPUs accelerators efficiently speed up the algorithm execution, allowing us to run the full 3D simulation in not more than a five-days wall time on our in-house high performance computing GPU cluster *octopus* [24], designed by the Scientific Computing Group at the Earth Sciences Institute and hosted by the University of Lausanne.

3.3 Material

Opalinus clay (shaly facies) is the Jurassic shale that is studied in the current work as the caprock representative. The shale contains 55-60% of clay (illite, kaolinite, chlorite, and smectite), 25-30% carbonate, 5-10% quartz, and 10-15% organic matter [25]. Interconnected porosity is 0.12, dominant pore throat diameter ~ 30 nm, and intrinsic permeability ~ 10^{-21} - 10^{-20} m^2 [4]. If preserved properly after coring, shale specimens have 80 – 90 % brine saturation, so the natural brine [26] was used as the pore fluid to minimize the chemical effect and its bulk modulus K_f is found to be 2.0 GPa, slightly less than the one for pure water.

The characteristic time for dissipation of the induced pore pressure in a specimen of length L drained at the two ends is on the order of $L^2/4c$, where c is the diffusion coefficient [27], which can be expressed from the permeability k, fluid viscosity μ, and the poroelastic parameters:

$$c = \frac{kB}{\mu\left(\frac{1}{K_d} - \frac{1}{K_s'}\right)} \tag{7}$$

Values of c for the tested shale are ~ 10^{-8} m^2/s for the case of brine saturation. The characteristic time scale for equilibration of the pore pressure inside the rock at the range of stresses applied is on the order of 10^{-5} s for 100-mm-long specimens (used in drained tests) and on the order of 10^{-4} s for the 35-mm-long specimen (used in the unjacketed test). In the latter case though, oil has partially penetrated into the unjacketed sample and increased the viscosity of the pore fluid, hence, the characteristic time scale for pressure dissipation. Finally, each new step in unjacketed test required 24 hours waiting period and the whole test took 15 days. At least 72 hours were spent between the consecutive steps during the drained loading.

4. Results and discussion

The unjacketed compression test provided constant (stress-independent) value of $K_s' = 8.9$ GPa for Opalinus clay after 15 days of gradual unloading from 60 MPa. Three different types of conventional triaxial tests were performed on the cylindrical shale specimens cored perpendicular to the bedding planes to measure the poroelastic parameters of the rock and evaluate its bulk viscosity. One of the specimens was tested at 24 ˚C under low mean stresses and pore pressures (around 2 MPa), approximately corresponding to the in-situ conditions at the Mont Terri underground rock laboratory from where the rock was recovered [25]. Full brine saturation in this case took about 75 days. Another specimen was gradually loaded to total isotropic stress of 10 – 30 MPa and saturated at pore fluid pressure of 8 MPa in 15 days, and its poroviscoelastic parameters were measured at 24 ˚C and 40 ˚C. Drained bulk modulus K and Skempton's B coefficient showed weak stress-dependence: $K = 2$ - 3 GPa and $B = 0.81 – 0.93$ for $p_e = 2 – 20$ MPa. Additionally, brine permeability of shale was measured by steady-state flow method and found to be strongly stress-dependent, changing by an order of magnitude for $p_e = 0.2 – 5$ MPa from ~ 10^{-20} m^2 to ~ 10^{-21} m^2.

The response of Opalinus clay was monitored after each B-check, while a constant isotropic total stress $\bar{p}$ was acting on the specimens. If the behavior of rock is purely poroelastic, application of constant total stress should not produce any pore fluid pressure perturbations. However, the pore pressure build-up occurred for fully saturated specimens at different initial total and pore pressures for all three tested cases (schematically shown in Fig. 1). Note that during the undrained loading when all-around stress is applied to the specimen, it is assumed that it affects the pore pressure immediately and equally inside all the pores. For the tested shale, it was found that pore pressure dissipation in the system takes a few tens of minutes and all further pore pressure changes should be associated with the time-dependent material behavior.

The observation times for the pore pressure build-up ranged from $4 \cdot 10^4$ to $1.5 \cdot 10^5$ seconds and provided approximately linear response given that the perturbations of total stress and temperature imposed by the loading system were very small. The effective stress does not appear to be the only governing parameter for the bulk viscosity for a number of sedimentary rock representatives, but rather it is the ratio between the pore pressure and total (isotropic) stress $p^f / \bar{p}$ [22]. The bulk viscosity η_ϕ of shale is calculated to be on the order of 10^{14} - 10^{15} Pa·s and have a decreasing trend with increasing $p^f / \bar{p}$ ratio (Fig. 2). Increase of temperature from 24 ˚C to 40 ˚C is found to have an insignificant effect on poroelastic parameters, but reduces the permeability by 40% and bulk viscosity by a factor of 2. Also, for the shale tested at low pressure, η_ϕ trend is different from the other two cases with a steeper decrease at p^f approaching $\bar{p}$, which may be related to the fact that the shale was subjected to lower than in situ stresses and behaved like underconsolidated material. Values of the bulk viscosity corresponding to the largest achieved $p^f / \bar{p}$ ratios for the three considered cases (low and high pressure hydrostatic compression at 24 ˚C and high pressure compression at 40 ˚C) along with the poroelastic parameters used for calculation are presented in Table 1.

Table 1. Material properties, poroelastic parameters, and bulk viscosity for the largest achieved $p^f / \bar{p}$ ratios for three studied cases.

Testing conditions	ϕ [-]	k [m^2]	K_d [GPa]	K_s' [GPa]	K_f [GPa]	B [-]	η_ϕ [Pa•s]
24 ˚C, $\bar{p}$ = 1.8 MPa p^f = 1.6 MPa	0.12	$3 \cdot 10^{-20}$	1.65	8.9	2.0	0.93	$2.2 \cdot 10^{14}$
24 ˚C, $\bar{p}$ = 15.5 MPa p^f = 12.8 MPa	0.12	$0.9 \cdot 10^{-20}$	2.2	8.9	2.0	0.90	$9.5 \cdot 10^{14}$
40 ˚C, $\bar{p}$ = 11.2 MPa p^f = 8.7 MPa	0.12	$0.5 \cdot 10^{-20}$	2.2	8.9	2.0	0.90	$4.6 \cdot 10^{14}$

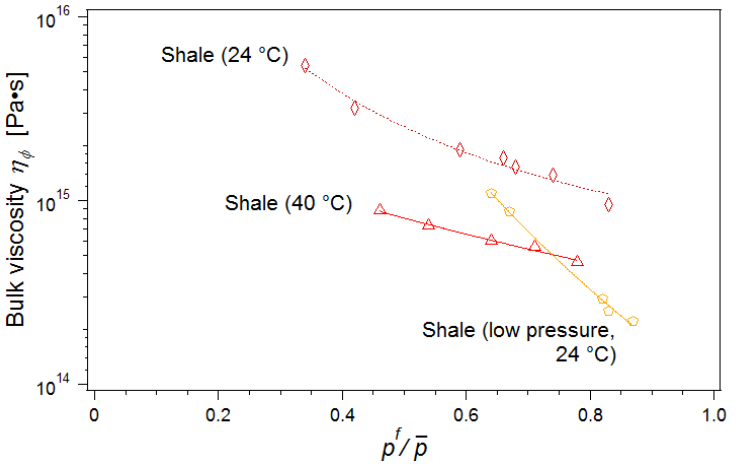

Fig 2. Calculated values of the bulk viscosity of shale plotted as functions of $p^f/\bar{p}$ ratio for the three considered cases: low pressure at 24 ˚C (orange pentagons), high pressure at 24 ˚C (maroon diamonds), and high pressure at 40 ˚C (red triangles).

Additionally, the bulk viscosity calculated for the shale at high pressure at 24 ˚C is plotted against the viscosity trends for two other sedimentary rocks: Berea sandstone and Apulian limestone tested at the same temperature [22] (Fig. 3). Increasing pore pressure at constant mean stress should lead to the increase in porosity if a geomaterial is deforming poroelastically. However, all the tested specimens were experiencing time-dependent compaction and measured volume strains were in agreement with porosity changes predicted by the presented poroviscoelastic relationships, which can be viewed as the model validation.

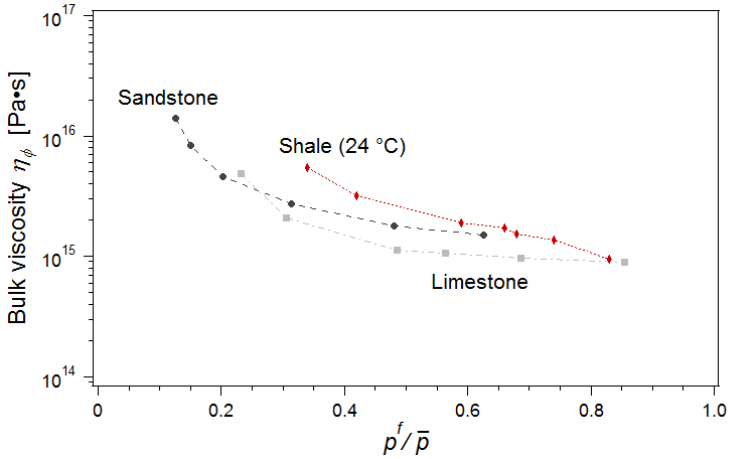

Fig 3. Bulk viscosity of Opalinus clay (maroon diamonds) in comparison to the trends of measured viscosities for Berea sandstone (dark grey circles) and Apulian limestone (light grey squares), all tested at 24 ˚C and plotted as functions of $p^f/\bar{p}$ ratio.

The measurements inferred from the lab are then used to constrain the important parameters of the numerical model. The initial setup (Fig. 4) used for the numerical simulation is a 3D cubic domain of viscoelastically deforming porous media saturated with pore fluid subject to gravity acceleration in the *z* (depth) coordinate. A high porosity horizontal ellipsoid is located at the first quarter of the total depth with porosity values twice higher than the background value. This setup should represent the analogy of a buoyant fluid plume, thus an elevated porosity

anomaly, located in a less permeable and less porous reservoir. Porosity evolution through time can be predicted and used to estimate the time and length scale representative for this wave propagation phenomenon.

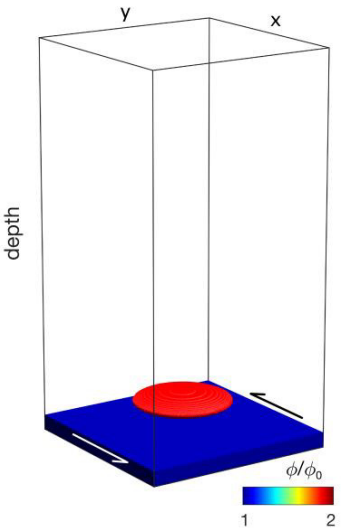

Fig 4. The setup used to model two-phase flow. The resolution is 500 x 500 x 1000 grid points in respectively *x*, *y*, and *z* (depth) dimensions. The domain was decomposed into 64 subdomains, each of them computed on a Nvidia Titan X GPU.

The outcome of the numerical simulations show elongated pipe features developing over time due to highly focused fluid flow through the deforming porous media (Fig. 5). The channel formation, and thus asymmetry in decompaction versus compaction rates is the result of viscosity dependence on $p^f/\overline{p}$ ratio. The effective viscosity drops in region where the pore fluid pressure gets closer to the total stress (red areas on the channel tip in Fig. 5). The created channels are referred to porosity waves, as the solid grains only get displaced very locally, allowing the fluid to go through the porous media in a wave like motion. The associated fluid pressure (Fig. 5) and its gradient will tend to move fluid from the near channel region into the channels. This mechanism enhances the self-sustainability of the porosity wave by providing significant amount of surrounding fluid to flow into the channel. The surrounding fluid being expelled from the near channel areas, the walls of the pipe compact as result of mass balance. The resulting channels wall bulk and shear viscosities increase, freezing their shape over time. The expression of this mechanism in natural system such shallow reservoirs can be related to seismic chimneys visible on seismic surveys cross section [14, 23].

Using the laboratory data on shale behavior, we can scale the numerical simulation in order to predict propagation velocities of the high porosity, thus high permeability channels. Permeability increase inside the channels is of more than three orders of magnitude, enabling pore fluid or brine to travel with a vertical speed proportionally to permeability increase (i.e. three orders of magnitude), instead of the background Darcian flow regime. The characteristic time t^* and length L^* are given by

$$t^* = \sqrt{\frac{\eta_\phi \mu}{k}} (\Delta\rho g)^{-1} \tag{8}$$

$$L^* = \sqrt{\frac{\eta_\phi k}{\mu}} \tag{9}$$

The travelling velocity for the porosity waves through the domain (in meters per year) can be computed as

$$V_{porosity\_wave} = \frac{L_{run} \cdot L^*}{t_{run} \cdot t^*} 3600 \cdot 24 \cdot 365 \quad \text{[m/year]} \tag{10}$$

where L_{run}/t_{run} is the dimensionless velocity obtained from the numerical simulation. Finally, the porosity wave velocity calculated using the poroviscoelastic properties of Opalinus clay appears to be on the order of centimeters per year for a very low permeable (~10^{-20} m^2) formation.

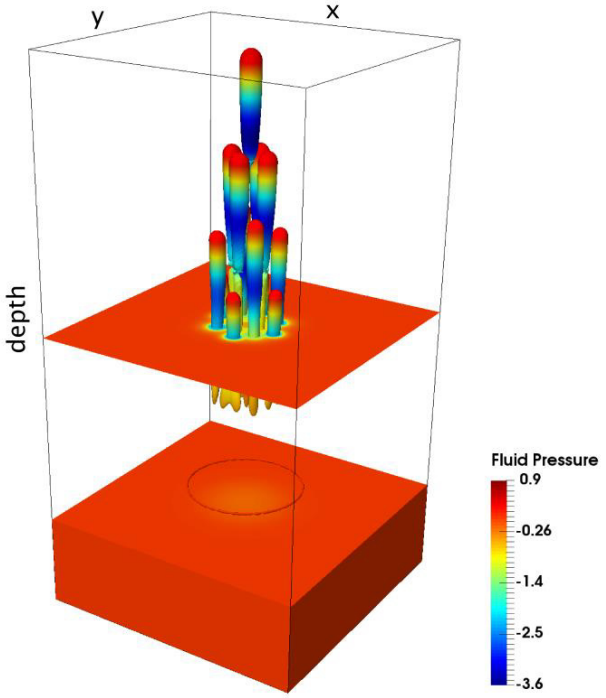

Fig 5. Fluid pressure values plotted on top of the isosurface values of normalised porosity equal to 4 as evolving form the initial high porosity ellipsoid (Fig.1) after dimensionless time of 0.024. Low fluid pressure values are observed within the high porosity channels. Box dimensions are 30 x 30 x 60 compaction lengths in *x*, *y*, and *z* directions respectively, or a numerical resolution of 500 x 500 x 1000 grid points. The visualisation is performed in parallel on 64 Titan X GPUs using the ParaView software in a remote client-server configuration on the *octopus* GPU cluster.

5. Conclusions

We show that viscous effect should not be excluded when assessing long-term behavior of clay-rich materials, such as shales. The modeling results using parameters from the laboratory experiments on low-permeable shale predict that nonlinear porosity-dependent permeability can increase up to three orders of magnitude within the porosity waves. Long-term projections for storage behavior should therefore include time-dependent (viscous) deformation of the potential caprocks.

Laboratory measurements performed to obtain both the permeability and viscosity values for the clay-rich rock types dramatically influence the prediction for the relevance of in-channel formation and propagation. Orders of magnitude changes in permeability will lead to proportionally faster or slower propagation velocities, as this quantity scales the dimensionless velocity of the model. Significantly low effective viscosity values obtained from the laboratory experiments dramatically decrease the characteristic propagation time of the fluid focusing instabilities. This might lead to the generation and propagation of high permeability tubular features in an operational time scale. The viscous or creep effect should therefore be considered while assessing storage integrity, especially for systems where clay-rich caprock formations are investigated. Under certain conditions, creeping ductile rock may locally flow away, leading to the formation of the vertical pipes of high permeability and porosity.

Acknowledgements

Opalinus clay cores were provided by Swisstopo in the framework of Mont Terri Project, CS-C experiment. R. Makhnenko acknowledges the support from SCCER-SoE (Switzerland) grant KTI.2013.288 and Swiss Federal Office of Energy (SFOE) project CAPROCK #810008154.

References

[1] IEAGHG. Caprock systems for CO_2 geological storage. IEA Environmental Projects Ltd 2011.
[2] Amann-Hildenbrand A, Bertier P, Busch A, Krooss BM. Experimental investigation of the sealing capacity of generic clay-rich caprocks. International Journal of Greenhouse Gas Control 2013;19:620-641.
[3] Boulin PF, Bretonnier P, Vassil V, Samouillet A, Fleury M, Lombard J-M. Sealing efficiency of caprocks: Experimental investigation of entry pressure measurement methods. Marine and Petroleum Geology 2013;48:20-30.
[4] Makhnenko RY, Vilarrasa V, Mylnikov D, Laloui L. Hydromechanical aspects of CO_2 breakthrough into clay-rich caprocks. Energy Procedia 2017 (this issue).
[5] Simon NSC. Compaction Driven Flow in Porosity Waves - A Threat to Caprock Integrity? Third EAGE CO2 Geological Storage Workshop 2012.
[6] Zhang C-L, Rothfuchs T, Su K, Hoteit N. Experimental study of the thermohydro-mechanical behaviour of indurated clays. Physics & Chemistry of Earth 2007; 32:957 – 965.
[7] Yang DS, Bornert M, Chanchole S. Experimental investigation of the delayed behaviour of unsaturated argillaceous rocks by means of Digital Image Correlation techniques. Applied Clay Sciences 2011; 54, 53–62.
[8] Sone H, Zoback MD. Time-dependent deformation of shale gas reservoir rocks and its long-term effect on in-situ state of stress. International Journal of Rock Mechanics & Mining Sciences 2014; 69:120-132.
[9] Elsworth D, Yasuhara H. Short-timescale chemo-mechanical effects and their influence on transport properties of fractured rock. Pure & Applied Geophysics 2006; 163:2051-2070.
[10] Bürgmann R, Dresen G. Rheology of the lower crust and upper mantle: Evidence from rock mechanics, geodesy, and field observations. Annual Review of Earth and Planetary Sciences 2008; 36(1):531.
[11] Brantut N, Heap MJ, Meredith PG, Baud P. Time-dependent cracking and brittle creep in crustal rocks: A review. Journal of Structural Geology 2013; 52:17-43.
[12] Connolly JAD, Podladchikov YY. An analytical solution for solitary porosity waves: dynamic permeability and fluidization of nonlinear viscous and viscoplastic rock. Geofluids 2015; 15(1 – 2):269 – 292.
[13] Yarushina VM, Podladchikov YY, Connolly JAD. (De)compaction of porous viscoelastoplastic media: Solitary porosity waves. Journal of Geophysical Research Solid Earth 2015; 120:4843-4862.
[14] Räss L, Yarushina VM, Simon NS, Podladchikov YY. Chimneys, channels, pathway flow or water conducting features-an explanation from numerical modelling and implications for CO_2 storage. Energy Procedia 2014; 63:3761-3774.
[15] Yarushina VM, Podladchikov YY. (De)compaction of porous viscoelastoplastic media: Model formulation, Journal of Geophysical Research Solid Earth 2015; 120:4146–4170.
[16] Wang HF, Theory of Linear Poroelasticity with Applications to Geomechanics and Hydrogeology. Princeton University Press 2000.
[17] Connolly JAD, Podladchikov YY. Decompaction weakening and channeling instability in ductile porous media: Implications for asthenospheric melt segregation. Journal of Geophysical Research Solid Earth 2007; 112:B10.
[18] Detournay E, Cheng A. Fundamentals of poroelasticity. In Fairhurst C (ed.) Chap. 5 in Comprehensive Rock Engineering: Principles, Practice and Projects, Vol. II, Analysis and Design Methods, Pergamon Press, Oxford 1993; pp. 113 – 171.
[19] Skempton AW. The pore-pressure coefficients A and B. Geotechnique 1954; 4:143-147.
[20] Makhnenko RY, Labuz JF. Elastic and inelastic deformation of fluid-saturated rock. Philosophycal Transactions of Royal Society A 2016; 374:20150422.
[21] Makhnenko RY, Labuz JF. Saturation of porous rock and measurement of the *B* coefficient. In Proceedings of the 47th U.S. Rock Mechanics/ Geomechanics Symposium, San Francisco, CA 23-26 June 2013; paper No. 468.
[22] Makhnenko RY, Podladchikov YY. Experimental poroviscoelasticity of common sedimentary rocks. In preparation 2017.
[23] Räss L, Yarushina V, Duretz T, Podladchikov Y. High-resolution numerical modeling to resolve the dynamics of pipe structures in porous media. EAGE ECMOR X conference 2016, Amsterdam.
[24] Scientific Computing Group, specification of the octopus GPU cluster. 2015: http://wp.unil.ch/geocomputing/computing-systems/octopus/
[25] Bossart P. Characteristics of the Opalinus Clay at Mont Terri. 2012: http:/mont-terri.ch/internet/montterri/de/home/geology/key_characteristics.html.
[26] Pearson FJ. PC experiment: recipe for artificial pore water. Mont Terri Project, Technical Note 2002-17.
[27] Zimmerman RW. Compressibility of sandstones. Elsevier, New York 1991.